

Photoemission oscillation in epitaxially grown van der Waals β-In_2Se_3/WS_2 heterobilayer bubbles

Jiyu Dong(董继宇), Kang Lin(林康), Congpu Mu(牟从普), Zhiyan Jia(贾智研), Jin Xu(徐瑾), Anmin Nie(聂安民), Bochong Wang(王博翀), Jianyong Xiang(向建勇), Fusheng Wen(温福昇), Kun Zhai(翟昆), Tianyu Xue(薛天宇), and Zhongyuan Liu(柳忠元)

Citation: Chin. Phys. B, 2021, 30 (**11**): 117901. DOI: 10.1088/1674-1056/ac272f
Journal homepage: http://cpb.iphy.ac.cn; http://iopscience.iop.org/cpb

What follows is a list of articles you may be interested in

Transport properties of doped Bi_2Se_3 and Bi_2Te_3 topological insulators and heterostructures

Zhen-Hua Wang(王振华), Xuan P A Gao(高翾), Zhi-Dong Zhang(张志东)
Chin. Phys. B, 2018, 27 (**10**): 107901. DOI: 10.1088/1674-1056/27/10/107901

Graphene/Mo_2C heterostructure directly grown by chemical vapor deposition

Rongxuan Deng(邓荣轩), Haoran Zhang(张浩然), Yanhui Zhang(张燕辉), Zhiying Chen(陈志蓥), Yanping Sui(隋妍萍), Xiaoming Ge(葛晓明), Yijian Liang(梁逸俭), Shike Hu(胡诗珂), Guanghui Yu(于广辉), Da Jiang(姜达)
Chin. Phys. B, 2017, 26 (**6**): 067901. DOI: 10.1088/1674-1056/26/6/067901

In-situ spectroscopic studies and interfacial engineering on FeSe/oxide heterostructures: Insights on the interfacial superconductivity

Peng Rui, Xu Hai-Chao, Feng Dong-Lai
Chin. Phys. B, 2015, 24 (**11**): 117902. DOI: 10.1088/1674-1056/24/11/117902

Mn overlayers on PbTe (111): Substitutional adsorption and interface formation

Wu Hai-Fei, Zhang Han-Jie, Lu Yun-Hao, Yan Yong-Hong, Li Hai-Yang, Bao Shi-Ning, He Pi-Mo
Chin. Phys. B, 2014, 23 (**12**): 127901. DOI: 10.1088/1674-1056/23/12/127901

Photoemission oscillation in epitaxially grown van der Waals β-In_2Se_3/WS_2 heterobilayer bubbles*

Jiyu Dong(董继宇)[1,†], Kang Lin(林康)[1,†], Congpu Mu(牟从普)[1,2,‡], Zhiyan Jia(贾智研)[1], Jin Xu(徐瑾)[2], Anmin Nie(聂安民)[1], Bochong Wang(王博翀)[2], Jianyong Xiang(向建勇)[1,§], Fusheng Wen(温福昇)[1], Kun Zhai(翟昆)[1], Tianyu Xue(薛天宇)[1], and Zhongyuan Liu(柳忠元)[1]

[1] *Center for High Pressure Science (CHiPS), State Key Laboratory of Metastable Materials Science & Technology, Yanshan University, Qinhuangdao* 066004, *China*

[2] *Key Laboratory of Microstructure Materials Physics of Hebei Province, School of Science, Yanshan University, Qinhuangdao* 066004, *China*

(Received 12 August 2021; revised manuscript received 8 September 2021; accepted manuscript online 16 September 2021)

Thin films of millimeter-scale continuous monolayer WS_2 have been grown on SiO_2/Si substrate, followed by the deposition of β-In_2Se_3 crystals on monolayer WS_2 to prepare In_2Se_3/WS_2 van de Waals heterostructures by a two-step chemical vapor deposition (CVD) method. After the growth of In_2Se_3 at elevated temperatures, high densities of In_2Se_3/WS_2 heterostructure bubbles with monolayer to multilayer β-In_2Se_3 crystals atop are observed. Fluorescence of the resultant β-In_2Se_3/WS_2 heterostructure is greatly enhanced in intensity upon the formation of bubbles, which are evidenced by the Newton's rings in optical image owing to constructive and destructive interference. In photoluminescence (PL) mapping images of monolayer β-In_2Se_3/monolayer WS_2 heterobilayer bubble, significant oscillatory behavior of emission intensity is demonstrated due to constructive and destructive interference. However, oscillatory behaviors of peak position are also observed and come from a local heating effect induced by an excitation laser beam. The oscillatory mechanism of PL is further verified by changing the exterior pressure of bubbles placed in a home-made vacuum chamber. In addition, redshifted in peak position and broadening in peak width are observed due to strain effect during decreasing the exterior pressure of bubbles.

Keywords: bubble, monolayer WS_2, heterostructure, In_2Se_3

PACS: 79.60.Jv, 33.20.Fb, 61.72.uj **DOI:** 10.1088/1674-1056/ac272f

1. Introduction

The optical, mechanical, and electrical properties of two-dimensional (2D) layered materials can be readily tuned via chemical doping, defect, or thickness reducing.[1–5] 2D transition-metal dichalcogenides (TMDCs) as one of the typical semiconductors possess novel physical properties for the potential application in a next generation photodetector, field-effect transistors, valleytronic devices.[6–8] The 2D van der Waals heterostructures consisted with stacking different 2D layered materials have novel properties beyond their individual counterparts, which provide opportunities in devices engineering.[9,10] For instance, the epitaxial grown multilayer β-In_2Se_3 on monolayer WS_2 have been shown to have the interlayers interaction effect constraining the phase transformation of adjacent few layers β-In_2Se_3.[11] Ultrahigh photo responsivity and detectivity of photodetectors are gained because of an acceleration of electron–hole separation and charge transfer owing to constructing lateral MoS_2 and WS_2 heterostructures.[12] In addition, various lateral and vertical 2D materials heterostructures have been constructed and investigated in physics and materials field.[13–15] It has been demonstrated that heterostructures based on TMDCs can provide a platform for tailoring the devices properties.

Recently, bubbles of monolayer or few layers 2D materials are created via various method and investigated in physics, chemistry, and devices.[1,5,16,17] A biaxial strain in bubbles can cause the direct-to-indirect band gap transition of few-layer TMDCs.[18] Strain localization excitons states formed a doughnut-like pattern around the nanoscale bubbles of monolayer WSe_2 and MoS_2 at room temperature.[19,20] Moreover, optical properties and lattice vibrations of graphene and TMDCs are sensitive with strain in material. Photoluminescence (PL) and Raman spectra oscillations can be found across graphene, monolayer WS_2, and few layer WSe_2 bubble profile due to light interference.[1,11,16] In addition, PL of monolayer WS_2 is sensitive with strain, electric filed, and temperature. Monolayer WS_2 has a potential application for photodetectors due to strong PL with narrower emission bandwidth. Although properties of single crystal monolayer WS_2

*Project supported by the National Natural Science Foundation of China (Grant Nos. 51732010 and 51972280), the Natural Science Foundation of Hebei Province, China (Grant No. E2019203233), the Research Program of the College Science & Technology of Hebei Province, China (Grant No. ZD2020121).

†These authors contributed equally to this work.

‡Corresponding author. E-mail: congpumu@ysu.edu.cn

§Corresponding author. E-mail: jyxiang@ysu.edu.cn

© 2021 Chinese Physical Society and IOP Publishing Ltd

bubbles have been investigated, there have not been reported about heterostructure bubbles of a millimeter-scale continuous monolayer polycrystalline WS_2 and other 2D layer materials so far.

In this paper, vertical β-In_2Se_3/monolayer WS_2 heterostructures were grown via a two-step chemical vapor deposition (CVD) and heterostructure bubbles on SiO_2/Si substrate were created during the growth of β-In_2Se_3 due to a high-temperature treatment. Characteristics of β-In_2Se_3/monolayer WS_2 heterostructure bubbles are investigated via optical and fluorescence (FL) images, Raman and PL spectra. The oscillatory behaviors are presented in mapping images of PL and Raman spectra of monolayer β-In_2Se_3/monolayer WS_2 heterostructure bubbles due to the constructive and destructive interference. The mechanism for oscillatory behaviors of PL intensity, position, and width are elucidated via changing an exterior pressure of bubble. In addition, strain effect in PL position and width is also observed during the gradual decrease of exterior pressure of bubbles.

2. Experimental section

2.1. Thin film of millimeter-scale continuous monolayer WS_2

Thin films of millimeter-scale continuous monolayer WS_2 were grown on p-type silicon wafer with 300 nm in thickness of SiO_2 CVD method in a two-zone home-made tube furnace. As schematically shown in Fig. S1, precursors of sulfur powder (Alfa Aesar, purity 99.999%) of 1.2 g and WO_3 powder of 2 g (Alfa Aesar, purity 99.99%) were placed in two separated Al_2O_3 crucibles located downstream at the low and high temperature zones, respectively. During the growth, the low and high temperature zones were set at 180 °C and 950 °C, respectively, and the sulfur and WO_3 vapor were carried to SiO_2/Si substrate via a highly pure Ar gas at a flow rate of 50 sccm. After a growth time of 50 minutes, thin films of millimeter-scale continuous monolayer WS_2 were successfully grown on SiO_2/Si wafers.

2.2. In_2Se_3/monolayer WS_2 heterostructure bubbles

The β-In_2Se_3/monolayer WS_2 heterostructure bubbles were created by using CVD method in a home-made three-zone tube furnace. Precursors of Se pellets of 0.08 g (Alfa Aesar, purity 99.999%) and In_2O_3 powder of 0.1 g (Alfa Aesar, purity 99.99%) were placed in two separated Al_2O_3 crucibles located downstream along the tube. The as-grown millimeter-scale continuous monolayer WS_2 films were served as 2D substrates and were downstream placed 5 cm away from the crucible of In_2O_3. During the growth, the temperatures were kept at 270, 640, and 620 °C for Se, In_2O_3, and substrate, respectively, and Se and In_2O_3 vapors were carried to the substrate via a 34 sccm mixed gas flow of H_2 and Ar. Similar to the previous reports that heat treatment of large area WS_2 or WSe_2 monolayers can help to create bubbles of monolayer,[11,16] In_2Se_3/monolayer WS_2 heterostructure bubbles with spherical cap were created during the growth of In_2Se_3 on WS_2 monolayer at 620 °C.

2.3. Characterizations

Optical and FL images were taken via a Leica microscope (DM4000M) equipped with FL accessory. PL and Raman spectra were collected in a confocal micro Raman microscope system (HR Evolution, JY Horriba, Japan) with an excitation of 532 nm and spot size of $\sim$ 1 μm in diameter. PL characterizations of bubbles under different exterior pressures are collected via a confocal micro Raman microscope system with a home-made vacuum chamber with a high-throughput optical window under an excitation of 532 nm focused on the center of bubble. Atomic force microscopy (AFM) measurement was performed on MultiMode 8 (Veeco Instruments Inc., USA) in a tapping mode. Structure was elucidated via an aberration-corrected scanning transmission electron microscopy (AC-STEM, FEI Themis Z STEM) operating at 300 kV.

3. Results and discussion

Figure 1(a) and figure S2 present the optical images and corresponding FL images of a typical as-grown thin film of monolayer WS_2 on SiO_2/Si substrate. It is clear that substrate is dominantly covered by monolayer WS_2 that is continuous over millimeter-scale. The polycrystalline thin film of monolayer WS_2 has a typical grain size of $\sim$ 100 μm, and the FL is greatly enhanced in intensity at the grain boundaries owing to the abundant structural defects.[21] The determined thickness of WS_2 from AFM height profile shown in Fig. S3 is $\sim$ 0.79 nm, which is consistent with previous results.[22,23] The high quality thin film of monolayer WS_2 enables the growth of layered β-In_2Se_3 crystals via CVD method. The optical images shown in Figs. 1(b) and 1(c) indicate that monolayer WS_2 is coated by layer structured β-In_2Se_3 crystals with different thicknesses and β-In_2Se_3/monolayer WS_2 heterostructures are obtained. Compared to the particles in the voids of monolayer WS_2 thin film, the well-defined multilayer β-In_2Se_3 crystals on WS_2 is indicating a preferential growth of the layered β-In_2Se_3 on 2D substrates. The high magnification optical image (Fig. 1(c)) also shows the absence of straight edge in morphology for the first and second layers of β-In_2Se_3 (*i.e.*, monolayer and bilayer In_2Se_3), which is consistent with the reported results.[11] Figure 1(d) shows the FL image of the monolayer WS_2 thin film after the growth of In_2Se_3. In comparison with the monolayer WS_2, the FL is significantly suppressed in intensity at the junction area

of In_2Se_3/WS_2. In addition, high density of brighter spots are evidenced in FL image, and fringes can be observed in spots with large size and are attributed to bubbles formed in monolayer WS_2 during growth of In_2Se_3.[11] It is also evident that bubbles of monolayer WS_2 have stronger FL signal than those of β-In_2Se_3/WS_2 heterostructure. From the variation in AFM height profile (inset of Fig. 1(e)) scanned along direction marked by the green line in Fig. 1(e), the thickness of monolayer β-In_2Se_3 is calculated to be ~ 1.01 nm, being in a good agreement with previous report for β-In_2Se_3.

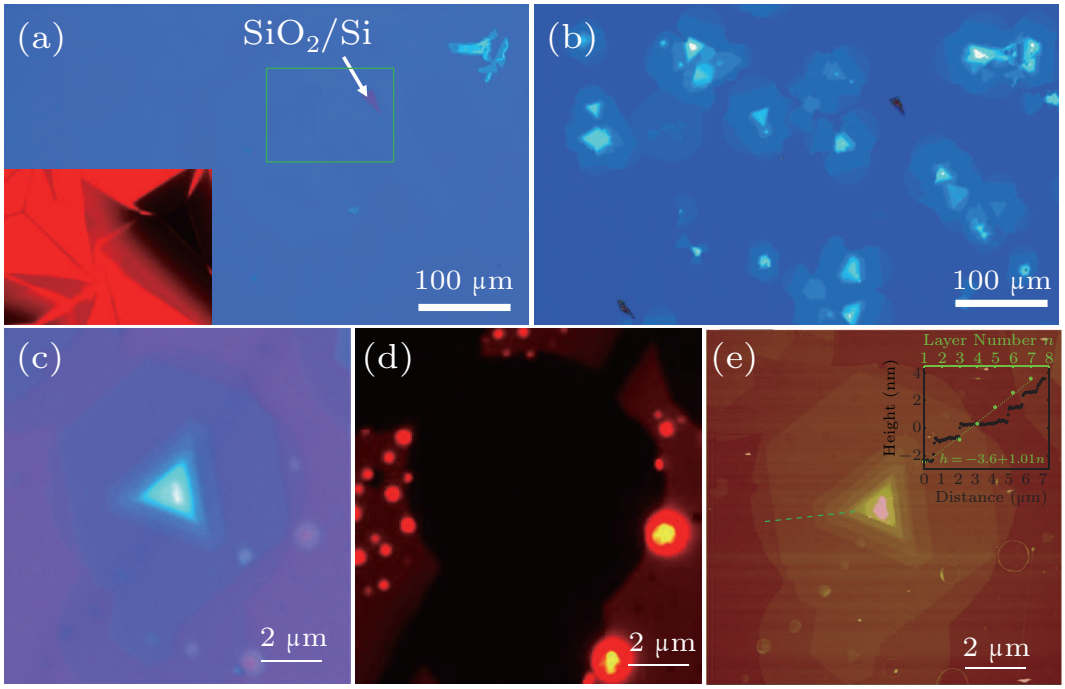


Fig. 1. Optical, FL, AFM characterizations of monolayer WS_2 before and after the growth of β-In_2Se_3: (a) optical image of millimeter-scale continuous monolayer WS_2 grown on SiO_2/Si substrate, the inset is FL image of green wireframe marked in optical image, indicating that millimeter-scale WS_2 is monolayer; (b) and (c) low- and high-magnification optical images of monolayer WS_2 covered with β-In_2Se_3, indicating forming β-In_2Se_3/monolayer WS_2 heterostructures; (d) FL image of β-In_2Se_3/monolayer WS_2 heterostructure, indicating that FL is suppressed after covering β-In_2Se_3, which is corresponding to panel (c); (e) AFM image of β-In_2Se_3/monolayer WS_2 heterostructure. The inset is the height profile from green wireframe, green dots come from AFM height profile, and green dashed line is linearly fitting the experiment dots according to the expression of $h = -3.6 + 1.01n$ (h is height and n is a layer number of In_2Se_3), indicating a thickness of ~ 1.01 nm for monolayer β-In_2Se_3.

Raman and PL measurements were carried out to characterize the as-grown WS_2 monolayer and In_2Se_3/WS_2 heterostructures transferred on TEM grid. Compared to the Raman spectra of monolayer WS_2, extra Raman bands are evidenced at the positions marked by the cyan for the β-In_2Se_3/WS_2 heterostructures, as shown in Fig. 2(a). The peaks located at ~ 110 cm^{-1} and 206 cm^{-1} are assigned to the A^1_{1g} and A^2_{1g} modes of β-In_2Se_3 crystal, respectively. According to previous work, Raman bands in intensity are very weak in intensity for the In_2Se_3 monolayer and bilayer.[11,24] The WS_2 monolayer possesses two characteristic peaks located at 353 cm^{-1} and 419 cm^{-1}, that are the in-plane mode of A_1 and out-of-plane mode of E′, respectively. No significant change occurs for the A_1 and E′ in frequency as well as intensity upon covering a layer of In_2Se_3 with a thickness from monolayer to few-layer.[11] When thickness of the atop β-In_2Se_3 increases up to 14 layers, the degenerated A_1 mode of monolayer WS_2 is observed to be split into two peaks due to the tensile strain preserved in thicker β-In_2Se_3 crystals grown at high temperatures.[11] It also indicates a strong coupling between monolayer WS_2 and multilayer In_2Se_3. Upon covering one layer of β-In_2Se_3 atop, PL is significantly decreased (by a factor of ~ 20) in intensity for monolayer WS_2, as shown in Fig. 1(d) and Fig. 2(b), and is even completely quenched with a 14-layer β-In_2Se_3 crystal atop. As shown in Fig. 2(c), conduction band minimum and the valence band maximum of monolayer WS_2 are higher than those of β-In_2Se_3, indicating a type-II alignment interface between β-In_2Se_3 and WS_2.[25–27] Due to a type-II alignment, the photo-excited electron in monolayer WS_2 is injected from conduction band of WS_2 to conduction band of β-In_2Se_3 and photo-excited holes will transfer from the valence band of β-In_2Se_3 to the valence band of WS_2 due to a type-II alignment of β-In_2Se_3/monolayer WS_2. Since the In_2Se_3 possesses an indirect bandgap, the suppression of PL in monolayer WS_2 after covering one layer of β-In_2Se_3 atop is due to the decrease of photo-excited electron–hole recombination rate. In addition, the quench of PL in monolayer WS_2 is predominantly attributed to that the photo-excited electron in monolayer WS_2 will transfer from monolayer WS_2 to thick β-In_2Se_3.

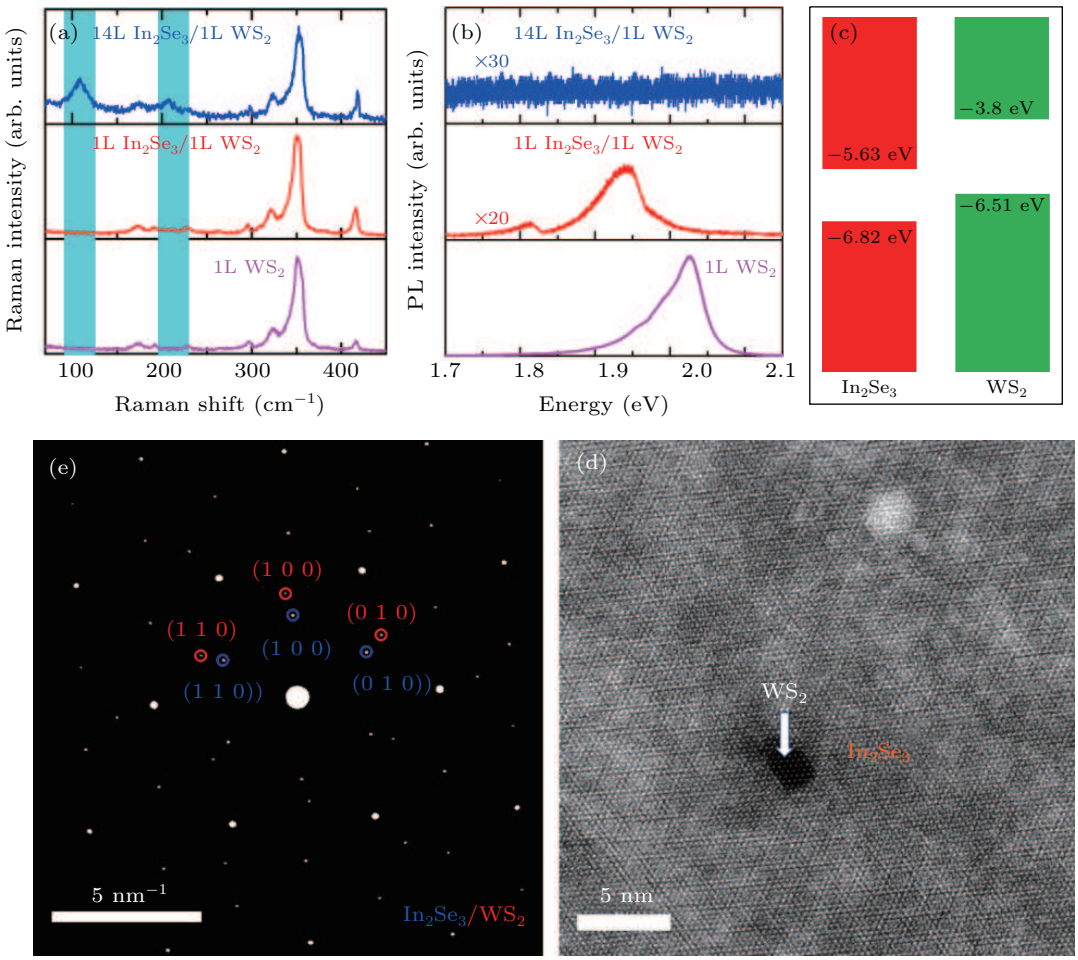


Fig. 2. (a) Raman and (b) PL characterizations of monolayer WS_2 before and after covered with 1L and 14L β-In_2Se_3 on TEM grid. (c) Band alignment of monolayer β-In_2Se_3 and monolayer WS_2. (d) SAED pattern and (e) atomic scale HAADF image of β-In_2Se_3/WS_2 heterobilayer.

In order to check the crystal structure and the crystallographic orientation of WS_2 and In_2Se_3, AC-STEM measurements were carried out on the heterobilayer of monolayer In_2Se_3/monolayer WS_2. Figure 2(d) presents a selected area electron diffraction (SAED) pattern of a typical heterobilayer β-In_2Se_3/WS_2. Two sets of diffraction patterns with sharp spots are evidenced owing to the high quality of WS_2 and In_2Se_3 crystal. The interplanar spacing of WS_2 and In_2Se_3 are 0.27 nm and 0.35 nm corresponding to the (100) lattice plane of 1H-WS_2 and β-In_2Se_3, respectively, which are consistent with previous results.[11,28,29] From the SAED pattern of the heterobilayer, it is clear that the monolayer β-In_2Se_3 crystal is nearly epitaxially grown on monolayer WS_2. Diffraction pattern of single crystal WS_2 is presented in SAED shown in Fig. 2(d) due to large grain size ($\sim$ 100 μm) in polycrystalline thin film of monolayer WS_2 (shown in Fig. 1(a) and Fig. S2). Figure 2(e) shows an atomic scale high angle annular dark field (HAADF) image of the β-In_2Se_3/WS_2 heterobilayer. Compared to the monolayer WS_2 (the dark domain as pointed out by the arrow), well-defined Moiré patterns can be observed in the domain of the heterobilayer owing to an interference of two sets mismatched lattices.

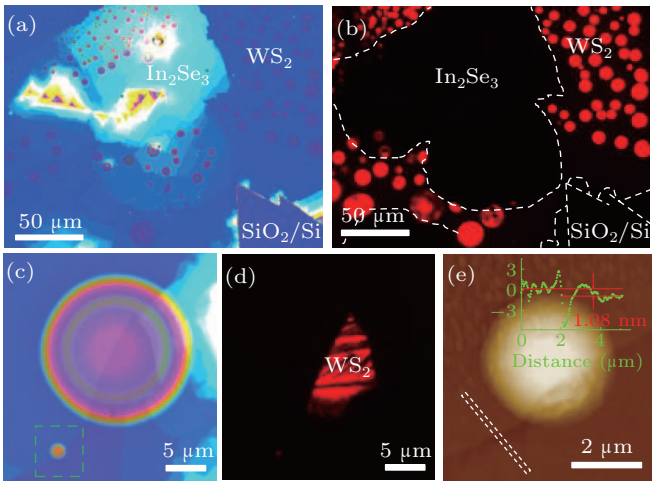


Fig. 3. (a) Optical and corresponding (b) FL images of monolayer WS_2 covered by In_2Se_3, (c) optical and corresponding (d) FL images of the bubble of In_2Se_3/monolayer WS_2 heterostructure, (e) AFM image of monolayer In_2Se_3/monolayer WS_2 heterostructure bubble (corresponding to the green dashed rectangle in panel (c)), inset is the height profile corresponding to the white line in panel (e).

Large number bubbles of In_2Se_3/monolayer WS_2 heterostructures were also created besides the monolayer WS_2 bubbles during the growth of β-In_2Se_3, as shown by the optical image and corresponding FL image of the as-grown β-In_2Se_3/monolayer WS_2 heterostructure in Figs. 3(a) and 3(b),

respectively. These bubbles have a widely distributed diameters range from few tens of micrometers down to the order of sub-micrometer or even smaller. Interference fringes with different color are clearly observed in bubbles with large diameter owing to the light interference, resembling a diffraction grating under the illumination of white light. β-In_2Se_3/WS_2 heterostructure bubbles can be formed with the top β-In_2Se_3 crystal varying from monolayer to more than 10 layers in thickness. The FL image clearly demonstrates an enhancement of FL in intensity upon the formation of bubbles of monolayer WS_2 as well as heterobilayer β-In_2Se_3/WS_2, though the FL intensity of the latter is much weaker. No evident FL is observed for the In_2Se_3/WS_2 heterostructure when layer number of β-In_2Se_3 is more than 1 layer in thickness. The enhancement in FL signal of bubbles is attributed to strain and/or the reduction in dielectric screening effect from the substrate.[30–32] Figures 3(c) and 3(d) show a high magnification optical image and corresponding FL image of a bubble spanning over monolayer WS_2, monolayer In_2Se_3/WS_2, and multilayers In_2Se_3/WS_2. Interference fringe rings are clearly presented in the contrast of optical and FL image owing to the interference of incident and reflected light at surface of the bubble, also signifying the suppression of FL of WS_2 in the heterostructure.

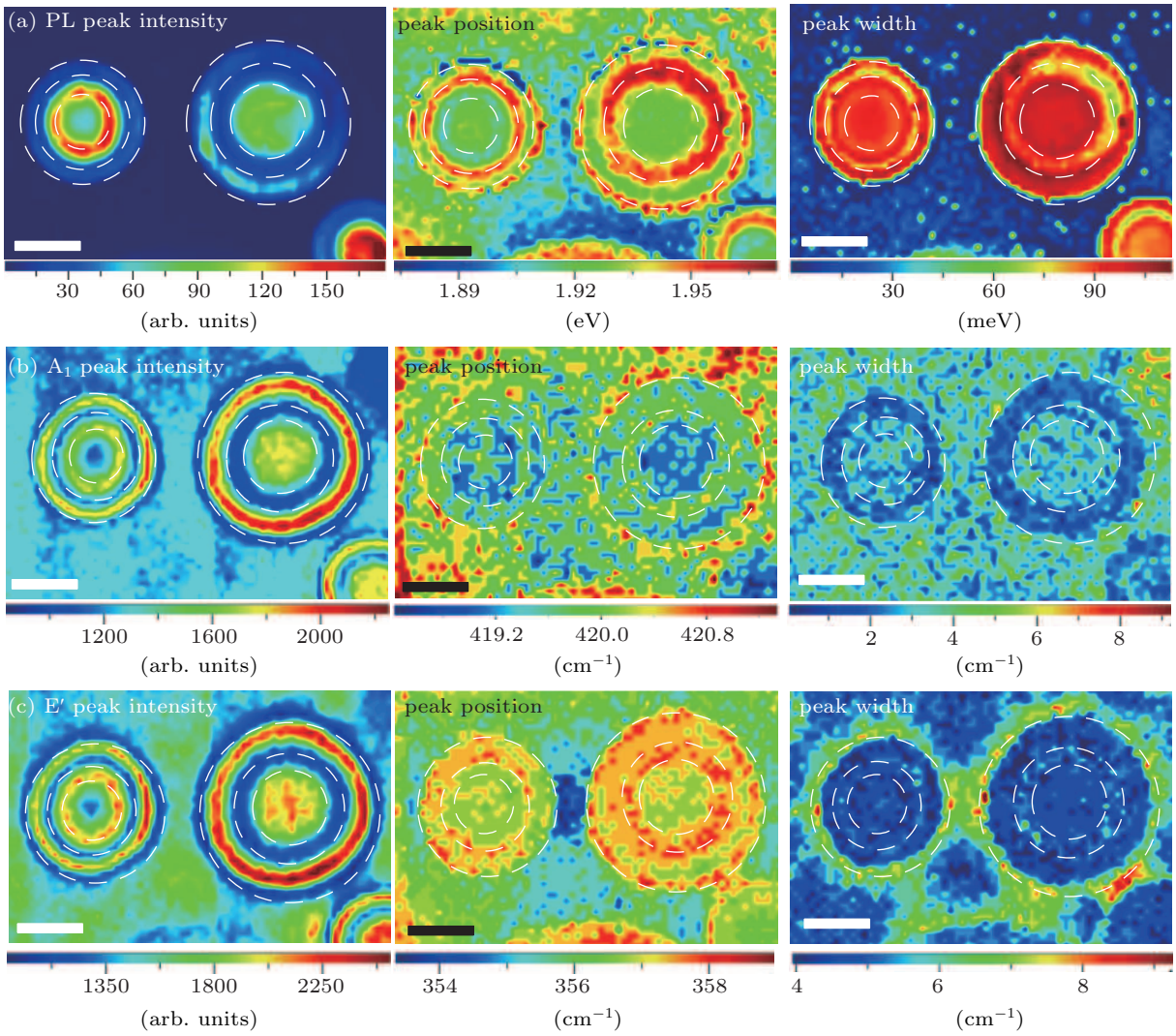


Fig. 4. PL and Ramana characterizations of In_2Se_3/WS_2 heterobilayer bubbles. (a) PL, (b) Raman A_1, and (c) Raman E′ peaks mapping images of intensity (left), position (middle), and width (right) collected via using laser light of 532 nm. Scales bars are 10 μm.

In order to check the morphology of bubble, AFM measurements were carried out on a bubble spanning over a monolayer WS_2 and a heterobilayer β-In_2Se_3/WS_2, as marked by the green dashed rectangle in Fig. 3(c). Figure 3(e) displays the AFM image and figure S4 presents a line profile across the top of bubble. The bubble demonstrates a well-defined spherical cap (with a lateral size of $\sim$ 4.6 μm and height of $\sim$ 164 nm). Inset in Fig. 3(e) is a height profile along the marked white line, a thickness $\sim$ 1.08 nm for the monolayer In_2Se_3 atop the monolayer WS_2 is clearly demonstrated.

Raman and PL measurements were carried out to characterize bubbles of In_2Se_3/WS_2 heterobilayer because the FL signal is nearly completely suppressed for heterostructure bubbles with the layer number of β-In_2Se_3 crystal more than one

layer in thickness. Two heterobilayer bubbles with different lateral sizes were chosen for the characterization, as marked by the green dashed rectangle on the optical image and corresponding FL image in Fig. S5, where Newton's rings and FL enhancement are clearly visible. Mapping images of peak intensity, position, and width for PL emission peak as well as for two characteristic Raman modes of the heterobilayer bubbles are presented in Fig. 4. From the center to the edge of bubbles, rings with periodic variation in intensity are clearly presented in the mapping of PL peak and Raman peaks of the A_1 and E′ modes (Figs. 4(a)–4(c)), sharing a spatial period depending on the bubble size. These rings with oscillatory intensity can originate from the interference of the constructive and destructive light in which the optical path difference varies as the light moving from the center to the edge of a bubble. The mappings of PL emission as well as for two characteristic Raman modes also display an oscillatory behaviors of the shift in peak position and broadening in peak width, and are attributed to the localized oscillatory heating induced by the periodic enhancement and suppression of the incident laser in intensity over the surface of bubbles.[1,16] In comparison with the phenomenon in the pure monolayer WS_2,[16] the oscillatory behavior in the PL emission and lattice vibrating is more profound in WS_2 for the In_2Se_3/WS_2 heterobilayer. This is attributed to lower thermal diffusivity in the In_2Se_3/WS_2 heterobilayer than of the monolayer WS_2 owing to the much lower thermal conductivity of monolayer β-In_2Se_3 (< 4 W/m·K) than that of monolayer WS_2 (~ 60 W/m·K).[33,34]

The interference phenomena at the surface of bubble depends on the optical path difference which is very sensitive to the bubble size (as shown in Fig. 4) and the pressure balancing the interior and exterior gas of the bubble.[35] By placing the In_2Se_3/WS_2 heterobilayer bubble into a home-made vacuum chamber, it tends to be gradually inflated when the vacuum chamber is subjected to a slow purging with a pump. Meanwhile, a tensile strain owing to the inflation of the bubble can be precisely generated,[1] which was used to finely tune the properties of monolayer WS_2 via strain.[36] Figure 5 presents the PL collected at center position of the β-In_2Se_3/WS_2 heterobilayer bubble subject to different exterior pressures. Typical PL spectra of the heterobilayer bubble at the exterior pressures of 100, 70, 50, 30, and 10 kPa are shown in Fig. 5(a), demonstrating a drastically modified emission characteristics of the monolayer WS_2 in the heterobilayer upon decreasing the exterior pressure. These spectra are deconvoluted by three Gaussian profiles (symbolized by X^0, X^1, and X^2) and parameters of intensity I_{peak} and emission energy E_{peak} are summarized in Fig. 5(b). An oscillatory behavior for I_{peak} and E_{peak} is clearly displayed, and superimposed on a nearly linear background for E_{peak} upon decreasing the exterior pressure of the heterobilayer bubble. The oscillation is resulted from the interference, while the persisting redshift of E_{peak} (linear background) is attributed to the increase of tensile strain during the inflation of the heterobilayer bubble, which is consistent with previous results on the counter part of monolayer WS_2.[32,36]

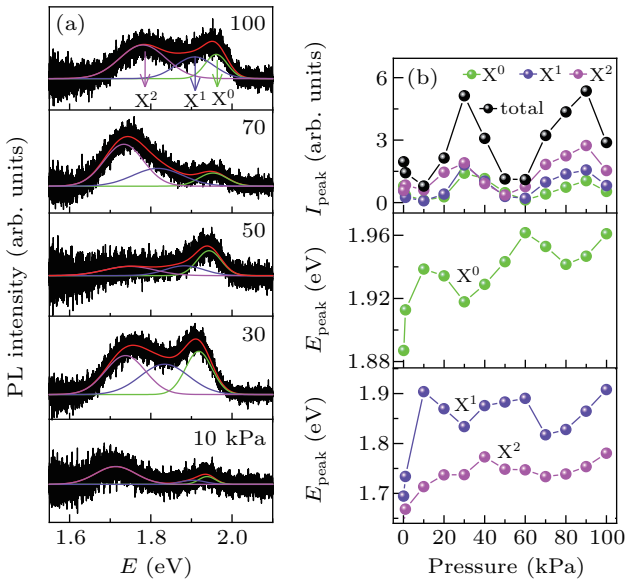


Fig. 5. PL characterizations for In_2Se_3/WS_2 heterobilayer bubble subjected to different exterior pressures with an excitation of 532 nm focused on the center of bubble. (a) PL spectra of the heterobilayer bubble at some typical exterior pressures of 10, 30, 50, 70, and 100 kPa. The spectra were deconvoluted by three Gaussian profiles (symbolized by X^0, X^1, and X^2). (b) Deconvoluted PL peak intensity I_{peak} and position E_{peak} as a function of the exterior pressure.

4. Conclusion

In conclusion, β-In_2Se_3 crystals are grown on a millimeter-scale continuous monolayer WS_2 attached on SiO_2/Si substrate via two-step CVD technique, preparing vertical van de Waals heterostructure. After the growth of β-In_2Se_3 at elevated temperatures, high density of In_2Se_3/WS_2 heterostructure bubbles with monolayer to multilayer β-In_2Se_3 crystals atop is observed. Newton rings are significantly observed in optical images of heterostructure bubbles due to constructive and destructive interference. In Raman and PL mapping images of β-In_2Se_3/WS_2 heterobilayer bubbles, significant oscillatory behaviors of emission intensity and peak positions are observed due to optical interference effect. However, oscillatory behaviors of peak position are also observed and come from a local heating effect induced by laser beam. The oscillatory mechanism of PL is further verified by changing the exterior pressure of bubbles. In addition, redshifted in peak positions are observed due to strain effect during decreasing the exterior pressure of bubbles.

References

[1] Huang Y, Wang X, Zhang X, Chen X, Li B, Wang B, Huang M, Zhu C, Zhang X, Bacsa W S, Ding F and Ruoff R S 2018 *Phys. Rev. Lett.* **120** 186104

[2] Zhang D, Gan L, Zhang J, Zhang R, Wang Z, Feng J, Sun H and Ning C Z 2020 *ACS Nano* **14** 6931

[3] Tripathi M, Lee F, Michail A, Anestopoulos D, McHugh J G, Ogilvie S P, Large M J, Graf A A, Lynch P J, Parthenios J, Papagelis K, Roy S, Saadi M A S R, Rahman M M, Pugno N M, King A A K, Ajayan P M and Dalton A B 2021 *ACS Nano* **15** 2520

[4] Mak K F, Lee C, Hone J, Shan J and Heinz T F 2010 *Phys. Rev. Lett.* **105** 136805

[5] Lloyd D, Liu X, Christopher J W, Cantley L, Wadehra A, Kim B L, Goldberg B B, Swan A K and Bunch J S 2016 *Nano Lett.* **16** 5836

[6] Sie E J, Lui C H, Lee Y H, Fu L, Kong J and Gedik N 2017 *Science* **355** 1066

[7] Jia Z, Dong J, Liu L, Xiang J, Nie A, Wen F, Mu C, Wang B, Zhai K, Yu Z, Kang M and Liu Z 2019 *Appl. Phys. Lett.* **115** 163104

[8] Yu Z, Ong Z Y, Li S, Xu J B, Zhang G, Zhang Y W, Shi Y and Wang X 2017 *Adv. Funct. Mater.* **27** 1604093

[9] Zhang D, Zeng Z, Tong Q, Jiang Y, Chen S, Zheng B, Qu J, Li F, Zheng W, Jiang F, Zhao H, Huang L, Braun K, Meixner A J, Wang X and Pan A 2020 *Adv. Mater.* **32** 1908061

[10] Jin C, Ma E Y, Karni O, Regan E C, Wang F and Heinz T F 2018 *Nat. Nanotechnol.* **13** 994

[11] Dong J, Liu L, Nie A, Xiang J, Zhai K, Wang B, Wen F, Mu C, Chen Y, Zhao Z, Gong Y, Tian Y and Liu Z 2020 *Appl. Phys. Lett.* **116** 021602

[12] Ye K, Liu L, Liu Y, Nie A, Zhai K, Xiang J, Wang B, Wen F, Mu C, Zhao Z, Gong Y, Liu Z and Tian Y 2019 *Adv. Opt. Mater.* **7** 1900815

[13] Nagler P, Ballottin M V, Mitioglu A A, Mooshammer F, Paradiso N, Strunk C, Huber R, Chernikov A, Christianen P C M, Schüller C and Korn T 2017 *Nat. Commun.* **8** 1551

[14] Britnell L, Ribeiro R M, Eckmann A, Jalil R, Belle B D, Mishchenko A, Kim Y J, Gorbachev R V, Georgiou T, Morozov S V, Grigorenko A N, Geim A K, Casiraghi C, Neto A H C and Novoselov K S 2013 *Science* **340** 1311

[15] Cai Z, Liu B, Zou X and Cheng H M 2018 *Chem. Rev.* **118** 6091

[16] Jia Z, Dong J, Liu L, Nie A, Xiang J, Wang B, Wen F, Mu C, Zhao Z, Xu B, Gong Y, Tian Y and Liu Z 2019 *Adv. Opt. Mater.* **7** 1801373

[17] Sanchez D A, Dai Z and Lu N 2021 *Trends Chem.* **3** 204

[18] Blundo E, Felici M, Yildirim T, Pettinari G, Tedeschi D, Miriametro A, Liu B, Ma W, Lu Y and Polimeni A 2020 *Phys. Rev. Research* **2** 012024

[19] Darlington T P, Carmesin C, Florian M, Yanev E, Ajayi O, Ardelean J, Rhodes D A, Ghiotto A, Krayev A, Watanabe K, Taniguchi T, Kysar J W, Pasupathy A N, Hone J C, Jahnke F, Borys N J and Schuck P J 2020 *Nat. Nanotechnol.* **15** 854

[20] Carmesin C, Lorke M, Florian M, Erben D, Schulz A, Wehling T O and Jahnke F 2019 *Nano Lett.* **19** 3182

[21] Jia Z, Hu W, Xiang J, Wen F, Nie A, Mu C, Zhao Z, Xu B, Tian Y and Liu Z 2018 *Nanotechnology* **29** 255705

[22] Feng S, Yang R, Jia Z, Xiang J, Wen F, Mu C, Nie A, Zhao Z, Xu B, Tao C, Tian Y and Liu Z 2017 *ACS Appl. Mater. Interfaces* **9** 34071

[23] Kobayashi Y, Sasaki S, Mori S, Hibino H, Liu Z, Watanabe K, Taniguchi T, Suenaga K, Maniwa Y and Miyata Y 2015 *ACS Nano* **9** 4056

[24] Mohapatra P K, Ranganathan K, Dezanashvili L, Houben L and Ismach A 2020 *Appl. Mater. Today* **20** 100734

[25] He J, Li T, Zhang L, He D, Wang Y, Ding H, Pan N and Zhao H 2018 *ACS Omega* **3** 11930

[26] Zhou B, Gong S J, Jiang K, Xu L, Zhu L, Shang L, Li Y, Hu Z and Chu J 2019 *J. Phys.: Condens. Mat.* **32** 055703

[27] Yang R, Liu L, Feng S, Liu Y, Li S, Zhai K, Xiang J, Mu C, Nie A, Wen F, Wang B, Zhang G, Gong Y, Zhao Z, Tian Y and Liu Z 2019 *ACS Appl. Mater. Interfaces* **11** 20979

[28] Chen Y, Gan L, Li H, Ma Y and Zhai T 2017 *Adv. Mater.* **29** 1603550

[29] Liu L, Dong J, Huang J, Nie A, Zhai K, Xiang J, Wang B, Wen F, Mu C, Zhao Z, Gong Y, Tian Y and Liu Z 2019 *Chem. Mater.* **31** 10143

[30] Buscema M, Steele G A, van der Zant H S J and Castellanos-Gomez A 2014 *Nano Research* **7** 561

[31] Lin Y, Ling X, Yu L, Huang S, Hsu A L, Lee Y H, Kong J, Dresselhaus M S and Palacios T 2014 *Nano Lett.* **14** 5569

[32] Liu Z, Amani M, Najmaei S, Xu Q, Zou X, Zhou W, Yu T, Qiu C, Birdwell A G, Crowne F J, Vajtai R, Yakobson B I, Xia Z, Dubey M, Ajayan P M and Lou J 2014 *Nat. Commun.* **5** 5246

[33] Zhou S, Tao X and Gu Y 2016 *J. Phys. Chem. C* **120** 4753

[34] Peimyoo N, Shang J, Yang W, Wang Y, Cong C and Yu T 2015 *Nano Research* **8** 1210

[35] Jia Z, Liu L, Li Y, Ye K, Dong J, Yu Z, Su C, Wang W, Xu D, Liu Z and Wang Z 2020 *J. Mater. Sci.* **55** 15857

[36] Wang Y, Cong C, Yang W, Shang J, Peimyoo N, Chen Y, Kang J, Wang J, Huang W and Yu T 2015 *Nano Research* **8** 2562